



Iron as Recyclable Metal Fuel: Unraveling Oxidation Behavior and Cyclization Effects Through Thermogravimetric Analysis, Wide-Angle X-ray Scattering and Mössbauer Spectroscopy

Carola Kuhn,^[a] Anna Knapp,^[a] Max P. Deutschmann,^[b] Jonas Spielmann,^[c] Steffen Tischer,^[d] Ulrike I. Kramm,^[c] Hermann Nirschl,^[b] and Olaf Deutschmann*^[a, d]

The carbon-free chemical storage and release of renewable energy is an important task to drastically reduce CO₂ emissions. The high specific energy density of iron and its recyclability makes it a promising storage material. Energy release by oxidation with air can be realized by the combustion of micron-sized iron powders in retro-fitted coal fired power plants and in fixed-bed reactors under milder conditions. An experimental parameter study of iron powder oxidation with air was conducted based on thermogravimetric analysis in combination with wide-angle X-ray scattering and Mössbauer spectroscopy.

In agreement with literature the oxidation was found to consist of a very fast initial oxidation of the outer particle layer followed by much slower oxidation due to diffusion of iron ions through the Fe₂O₃/Fe₃O₄ layer being the rate-limiting step. Scanning electron microscopy analysis of the iron particle before and after oxidation reveal a strong particle morphology transformation. This impact on the reaction was studied by cyclization experiments. Up to 10 oxidation-reduction cycles show that both, oxidation and reduction rates, increase strongly with cycling due to increased porosity.

Introduction

An important target for drastically reduced greenhouse gas emissions is the transformation of the energy sector from fossil fuels to solar and wind as primary energy sources. An increased share of renewable energies requires suitable energy carriers to ensure a stable energy supply and tradability. Hydrogen and ammonia are widely discussed chemical energy carriers, which however still face major obstacles in terms of the long-term storage of energy on the scale of TWh as well as handling and

safety.^[1–4] Another class of promising chemical energy carriers are metal fuels and in particular iron.^[5,6] Beside the high gravimetric energy density of iron (16.1 kWhL^{-1[7]}) compared to liquefied hydrogen (2.4 kWhL^{-1[8,9]}) and ammonia (3.8 kWhL^{-1[10]}), the main advantages of iron as metal fuel are the non-toxicity and the high abundance in the earth crust. Micron-sized iron powder can be combusted in retro-fitted coal-fired power plants for energy release.^[11,12] Recycling of the obtained iron oxides is possible by reduction with green hydrogen in areas with a surplus of renewable energies.^[13] The reduction of iron oxides with hydrogen is a process under consideration for green steel production and expected to gain importance in the future.^[14] Although the dry reforming of coke-oven gases presents a promising technology for reducing CO₂ emissions in the near term, the reduction of iron oxides with hydrogen holds long-term significance.^[15,16] The recycled iron powder can then be stored and shipped to places with high energy demand to close a carbon-free energy cycle.


First studies investigated the cycle efficiency of the overall process postulating a power-to-power energy efficiency ranging from 19% to 31%.^[17–20] The combustion of iron in a retro-fitted coal-fired power plant and the subsequent reduction have the advantage that the charging and discharging processes can be spatially decoupled. For stationary applications, Diego and Abanades^[21] proposed a new chemical looping fixed-bed reactor concept with iron as energy carrier, in which heat is released by oxidation with low oxygen concentrations, controlling the reaction rate by diffusion limitations to avoid hot spot formation.^[22] Recycling is conducted in the same reactor by reduction with hydrogen or another reducing gas e.g. syngas. The thermochemical energy storage is a second concept that is currently discussed. Here, the charging is realized by heating up


[a] C. Kuhn, A. Knapp, O. Deutschmann
 Institute for Chemical Technology and Polymer Chemistry
 Karlsruhe Institute of Technology (KIT)
 Engesserstr.20, 76131 Karlsruhe (Germany)
 E-mail: deutschmann@kit.edu

[b] M. P. Deutschmann, H. Nirschl
 Institute of Mechanical Process Engineering and Mechanics
 Karlsruhe Institute of Technology (KIT)
 Straße am Forum 8, 76131 Karlsruhe (Germany)

[c] J. Spielmann, U. I. Kramm
 Eduard-Zintl-Institute for Inorganic and Physical Chemistry
 Technical University Darmstadt
 Otto-Berndt-Str.3, 64287 Darmstadt (Germany)

[d] S. Tischer, O. Deutschmann
 Institute of Catalysis Research and Technology
 Karlsruhe Institute of Technology (KIT)
 Hermann-von-Helmholtz-Platz 1, 76344 Eggenstein-Leopoldshafen (Germany)

 Supporting information for this article is available on the WWW under <https://doi.org/10.1002/cssc.202400351>

 © 2024 The Authors. ChemSusChem published by Wiley-VCH GmbH. This is an open access article under the terms of the Creative Commons Attribution License, which permits use, distribution and reproduction in any medium, provided the original work is properly cited.

the energy storage material to very high temperatures, e.g. in concentrated solar power plants, leading to the release of O_2 .^[23,24]

Several studies focus on a detailed understanding of the oxidation of iron.^[25–27] Recent work describing the combustion of iron powders is based on kinetic data obtained from oxidation experiments of bulk iron^[28] as the oxidation behavior of iron slabs and strips has been studied in detail due to the importance of the reaction for the steel industry.^[29] For iron strips complete oxidation is only observed in large time scales, while for short time scales oxide layers growth can be analyzed. Pujilaksono et al.^[30] investigated the oxidation of iron strips with 5 vol.-% oxygen in nitrogen at 500 °C and 600 °C. For oxidation at 500 °C the oxide layer scale formation is characterized by an outer, thin layer of hematite (Fe_2O_3) and a thicker magnetite (Fe_3O_4) layer. With wüstite (FeO) being thermodynamically stable for $T > 570$ °C oxidation of iron strips at 600 °C is dominated by FeO formation.^[30,31] In contrast to iron slabs, iron particles in the micro- or nanometer range can be oxidized at elevated temperatures within a short time range.^[32,33] Korshunov^[33] studied the oxidation of iron nanopowder with an average particle diameter of $d_p^{avg} = 100$ nm and a micropowder with $d_p^{avg} = 45$ μm by thermogravimetric analysis. They conducted both isothermal (250 °C to 600 °C) and non-isothermal (10 K min⁻¹) experiments in air atmosphere. It could be shown that the onset of the oxidation is strongly shifted to lower temperatures with decreasing particle size.^[33] Additionally, decreasing the particle size leads to an accelerated reaction rate. Similar findings for the oxidation of various nanopowders and a micropowder were reported by Lysenko et al.^[34] and Zhang et al.^[35] This phenomenon can be elucidated by the development of a dense iron oxide layer, thereby transitioning the oxidation mode from the kinetic regime to the diffusion-limited regime.^[22,33]

Aside from the particle size, other aspects might influence the oxidation behavior such as the particle morphology and the agglomeration of particles. For a better understanding of the reaction mechanism information on the formation of reaction intermediates is very useful. This work contributes to the understanding of the oxidation and reduction of micron-sized iron/iron oxide particles with air and hydrogen, respectively. The focus is on elucidating the reaction mechanism, exploring morphological modifications of the particles, and assessing the impact of operation conditions. Isothermal and non-isothermal thermogravimetric experiments are conducted varying the experimental conditions heating rate, temperature and initial particle size. The particles were analyzed by scanning electron microscopy (SEM), wide-angle X-ray scattering (WAXS) and Mössbauer spectroscopy. Recyclability of the iron/iron oxide particles was investigated by repeated oxidation and reduction and characteristics of the particles were obtained.

Results and Discussion

In the first part the results of the oxidation of iron particles with air based on both non-isothermal and isothermal thermogravi-

metric analysis are presented and discussed taking into account the additional results from SEM, WAXS and Mössbauer spectroscopy. The utilization of two distinct analysis methods for examining the samples enables result validation. In addition, WAXS was employed for the qualitative analysis of the samples, forming the basis for the subsequent, more time-consuming analysis using Mössbauer spectroscopy to quantitatively determine the phase composition of selected samples. The second part presents the results of the cyclization experiments.

Oxidation

Non-Isothermal Thermogravimetric Analysis

The oxidation of the iron powder sample Fe23 was analyzed with TGA for heating rates of 2 Kmin⁻¹, 5 Kmin⁻¹ and 10 Kmin⁻¹. The results are shown in Figure 1. The oxidation starts at approximately 400 °C independent of the heating rate. For temperatures below 500 °C the oxidation rate is rather slow but increasing with rising temperature. The oxidation is slightly shifted to higher temperatures with increasing heating rate. For a heating rate of 2 Kmin⁻¹ a plateau is reached at 760 °C. With a heating rate of 10 Kmin⁻¹ this plateau is reached at 860 °C. Either complete oxidation or a significantly slowed reaction may be indicated by a stagnation of the mass change. However, this plateau is below the theoretically expected value of 143 % for all heating rates. WAXS analysis of reaction intermediates were carried out to verify whether the oxidation is complete and to receive detailed information on the course of the reaction.

For this purpose, the heating ramp was ended at temperatures of 500 °C, 600 °C, 700 °C, 800 °C, 900 °C and 1000 °C. After reaching the temperature, the sample was cooled in N_2 atmosphere to prevent further oxidation. Figure 2 shows the WAXS spectra of the oxidation of iron with a heating rate of

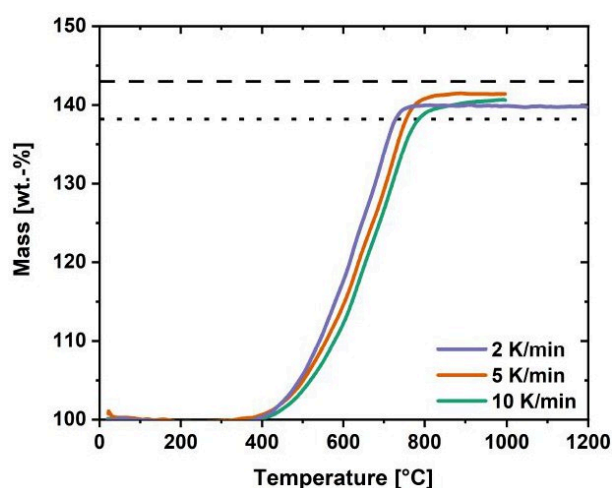


Figure 1. Thermogravimetric data of the oxidation of sample Fe23 in synthetic air with varying heating rates. The dotted line marks the theoretical mass gain reached by oxidation to Fe_3O_4 and the dashed line to complete oxidation to Fe_2O_3 .

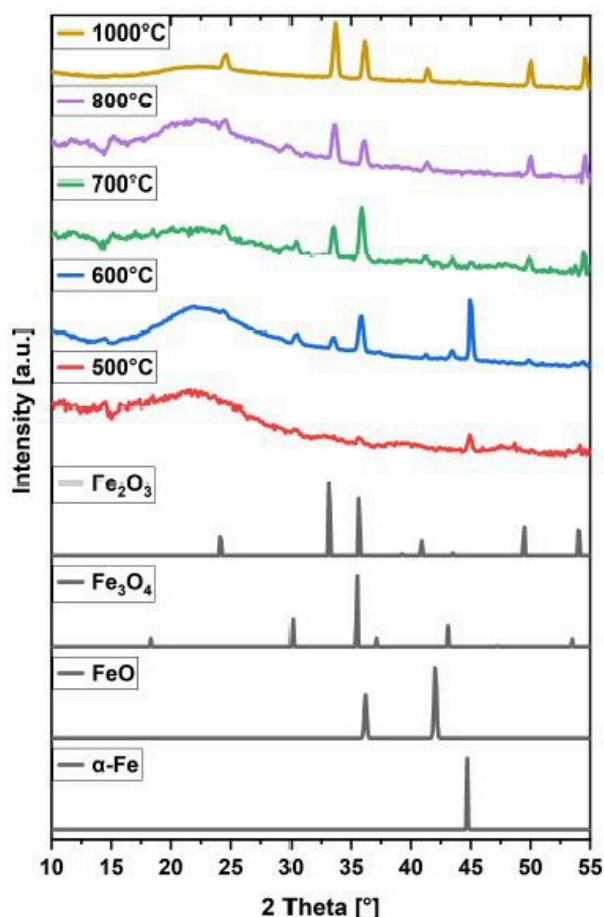


Figure 2. WAXS spectra of the oxidation of iron with a mean particle diameter of 23 with a heating rate of 10 K min^{-1} up to the temperatures 500°C , 600°C , 700°C , 800°C , 900°C and 1000°C with the reference spectra α -Fe, Fe_3O_4 , and α - Fe_2O_3 .

10 K min^{-1} from 500°C to 1000°C with the reference spectra of α -Fe, Fe_3O_4 and α - Fe_2O_3 . In the sample, which was oxidized up to 500°C , the scattering of the amorphous phase predominates and the spectra is therefore limited in its evaluability. The α -iron reflex can be identified. Smaller peaks, presumably due to iron oxides, stand out too little from the background noise to be accurately assigned. Oxidation up to 600°C leads to a mass increase of approximately 12%. The WAXS analysis shows interference peaks at 30° , 35.5° and 43° that can be assigned to Fe_3O_4 . The strong peak at 44.7° can be attributed to α -Fe and the small peak at 33° reveal that the formation of Fe_2O_3 has already started. At 700°C , all three phases, α -Fe, Fe_3O_4 , and α - Fe_2O_3 are present. Compared to 600°C , the α -Fe peak is less intense, but the interference peaks of the Fe_3O_4 and α - Fe_2O_3 oxides are stronger. At 800°C , the peaks can be assigned to the iron oxides Fe_3O_4 and Fe_2O_3 . Iron is no longer present at this temperature, so iron is completely oxidized between 700°C and 800°C . In addition, the inversion of the intensity ratio of the peaks at 33° and 35.5° indicates an increase in the ratio of Fe_2O_3 to Fe_3O_4 in the sample. At 1000°C , only the peaks of α - Fe_2O_3

are present showing that complete oxidation of iron to hematite is achieved.

Figure 3 displays the oxidation of iron particles with varying mean particle diameter and a heating rate of 10 K min^{-1} . The oxidation is shifted to higher temperatures with increasing particle size. For the smallest particles with a mean diameter of $23 \mu\text{m}$ the oxidation starts around 400°C while for iron particles with a mean particle diameter of $119 \mu\text{m}$ the onset of the oxidation is around 600°C . Until 690°C , sample Fe119 and Fe185 show a similar mass gain. The oxidation rate of sample Fe185 decreases for higher temperatures before it increases again for temperatures higher than 820°C . This effect can possibly be attributed to the fact that the sample has a proportion of smaller particles which are already oxidized at lower temperatures (Table 2 and Figure S1). Another effect might be the higher porosity of sample Fe185 compared to the other samples of iron particles, as can be deduced from the SEM images (Figure 17).

Furthermore, the oxidation behavior of the smallest iron particles Fe23 investigated differs from the oxidation of the larger iron particles. In contrast to the smallest particles, the oxidation of the larger iron particles can be divided into two stages. For the larger particles, the oxidation is initially slow and then becomes faster between 600°C and 700°C . The faster oxidation could be caused by a change in the reaction mechanism. Above a temperature of 570°C , wüstite is thermodynamically stable; at lower temperatures, no FeO is formed. In the oxidation of iron bars, the reaction rate below the wüstite formation limit is determined by the diffusion of iron ions through Fe_3O_4 . However, at higher temperatures, the ease of diffusion of iron ions through a developing FeO layer substantially enhances the rate of oxidation.^[36] Since the rate of oxidation of Fe70 and Fe119 increases in this temperature range, the formation of wüstite could be the reason for the two-step oxidation.

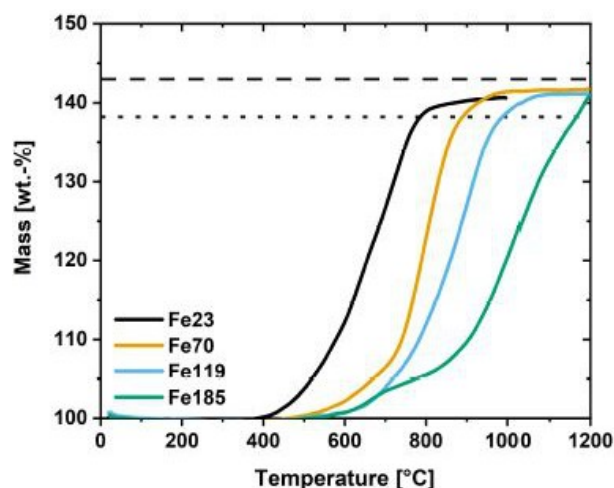


Figure 3. TGA of the oxidation of Fe23, Fe70, Fe119 and Fe185 with a heating rate of 10 K min^{-1} . The dotted line marks the theoretical mass gain reached by oxidation to Fe_3O_4 and the dashed line to complete oxidation to α - Fe_2O_3 .

Isothermal Thermogravimetric Analysis

The oxidation of sample Fe23 was investigated at temperatures from 400 °C to 900 °C. The resulting TGA curves are depicted in Figure 4. The isothermal oxidation is characterized by a fast initial oxidation followed by a strongly decelerated reaction rate. The oxidation degree reached within the initial oxidation phase increases strongly with increasing temperature. The initial oxidation leads to a mass increase of around 1% at 400 °C. Thereafter, no significant oxidation can be observed. In comparison to that, the oxidation at 500 °C leads to an initial mass increase of around 2% but the oxidation proceeds up to a mass gain of 8% after 60 min. A similar picture occurs for the oxidation at 600 °C. Here, the initial oxidation leads to a mass increase of roughly 7% within 2 minutes and a further mass increase of 13%. A total mass increase of 20% is achieved after 60 minutes. The comparison between 600 °C and 700 °C indicates a significant leap of the oxidation rate. At 700 °C around 27% mass increase are reached in the initial oxidation phase. After 45 min, a plateau is reached with a final mass growth of 41%. At 900 °C, iron is completely oxidized in the initial oxidation phase. Here, it requires 4 min to reach complete oxidation with a mass increase of 43%.

For a more detailed understanding of the oxidation process the samples obtained after oxidation for 60 min were analyzed by WAXS to determine the phase composition (Figure 5). The WAXS spectra of the sample oxidized at 400 °C shows a sharp peak that can be attributed to α -Fe. Furthermore, less intense peaks can be detected. However, these peaks do not stand out enough from the background noise to be clearly defined. This observation is in line with the results from thermogravimetric analysis, in which 1% increase in mass indicates the formation of small amounts of oxides. The spectra of the sample oxidized for 60 min at 500 °C shows peaks which can be attributed to

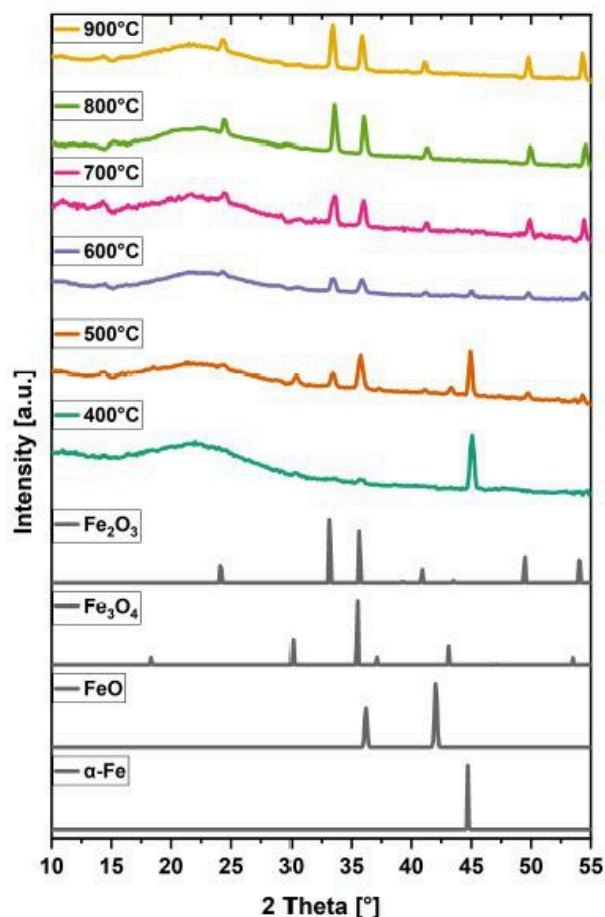


Figure 5. WAXS spectra of iron particles with a mean diameter of 23 μm oxidized for 60 min at temperatures from 400 °C to 900 °C and the reference spectra of α -Fe, Fe_3O_4 and α - Fe_2O_3 .

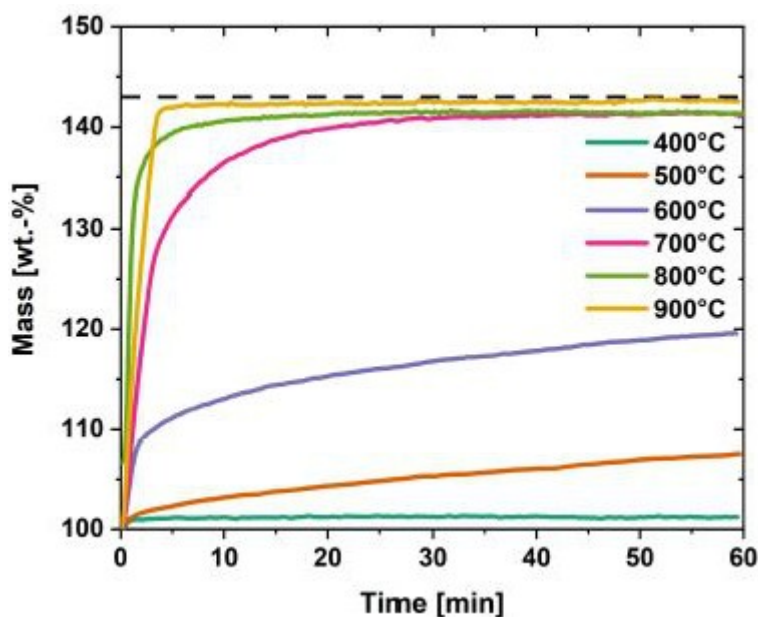


Figure 4. TGA of the isothermal oxidation of powder sample Fe23 with temperatures from 400 °C to 900 °C.

α -Fe, Fe_3O_4 and α - Fe_2O_3 . The ratio of magnetite to hematite can be determined by considering the ratio of the peaks at 33° and 35.5° . The reflex at 35.5° is the most intense reflection of Fe_3O_4 and overlaps with the reflection of α - Fe_2O_3 at 35.6° . Since the peak at 35.5° is generated by both magnetite and hematite, an increase in the intensity ratio of the peak at 33° to the peak at 35.5° indicates an increase in the mass ratio of hematite to magnetite. Considering this, it can be observed that the ratio of Fe_3O_4 to Fe_2O_3 decreases with increasing oxidation temperature. At 800°C and 900°C magnetite is not detected in the sample, indicating complete oxidation. A more detailed analysis of the obtained powder samples can be conducted by Mössbauer spectroscopy. Here, the phase composition is determined as depicted in Figure 6. The trend, which is already evident in the WAXS spectra, can be confirmed by Mössbauer spectroscopy. At 400°C a thin oxide layer consisting of Fe_3O_4 and Fe_2O_3 is formed. The amount of iron decreases from 400°C to 600°C while the amount of Fe_2O_3 increases. At 600°C the amount of Fe_2O_3 is nearly doubled compared to 500°C while the amount of Fe_3O_4 is slightly decreased. Additionally, small traces of FeO could be identified. The results obtained by Mössbauer spectroscopy confirm the complete oxidation at 800°C and 900°C , while at 700°C a small amount of Fe_3O_4 remains not completely oxidized. It's important to consider that the composition of the sample determined by Mössbauer spectroscopy indicates a higher degree of oxidation than the TGA results. Two factors contribute to this discrepancy. Firstly, the TGA measurements have an error of approximately 2%, and secondly, the possibility that the sample undergoes further oxidation after quenching. Another factor to consider is Mössbauer spectroscopy, where, for larger particles, outer shells may be weighted slightly higher due to the penetration depth of the radiation. This can lead to overrepresentation of higher oxides in the analysis, as oxidation is likely to start from the outer layers and progresses inward.

The isothermal oxidation was analyzed in detail for a temperature of 600°C . Here, experiments were performed up to

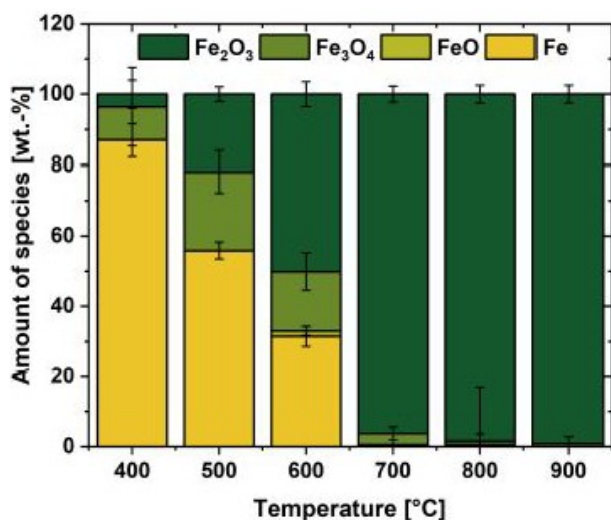


Figure 6. Phase composition of iron powder samples oxidized for 60 min at temperatures from 400°C to 900°C determined by Mössbauer spectroscopy.

15 min, 30 min, 45 min, 60 min, 120 min and 240 min to analyze the obtained reaction intermediates by WAXS and Mössbauer spectroscopy. The resulting WAXS spectra are shown in Figure 7. The respective TGA curve is shown in Figure S3. The oxidation at 600°C is very slow. After 4 h, a mass gain of only 26% can be achieved. The reflections in the spectra of the samples obtained after oxidation can be attributed to α -Fe, Fe_3O_4 and Fe_2O_3 . An increase in the ratio of hematite to magnetite with oxidation time can be observed as the peak area of the reflex at 33° increases relative to the reflex at 35.5° , which is associated to magnetite. In the samples oxidized for 2 h and 4 h only the reflexes of Fe and Fe_2O_3 can be identified unambiguously. The 4 h spectra shows a narrow elevation at 30° , which could be due to minor quantities of Fe_3O_4 . The presence of Fe_3O_4 in samples oxidized for longer time periods was confirmed through Mössbauer spectroscopy (Figure 8). The initial oxidation leads to the formation of Fe_3O_4 and Fe_2O_3 in comparable fractions. The amount of Fe decreases from 15 min to 30 min. However, as the oxidation proceeds, the amount of Fe does not change significantly. With increasing time, the amount of Fe_2O_3 increases, while the amount of Fe_3O_4 steadily decreases. In comparison to the WAXS analysis, Mössbauer spectroscopy is able to confirm the formation of FeO, although it is only formed in small amounts of around 1 % to 3 %.

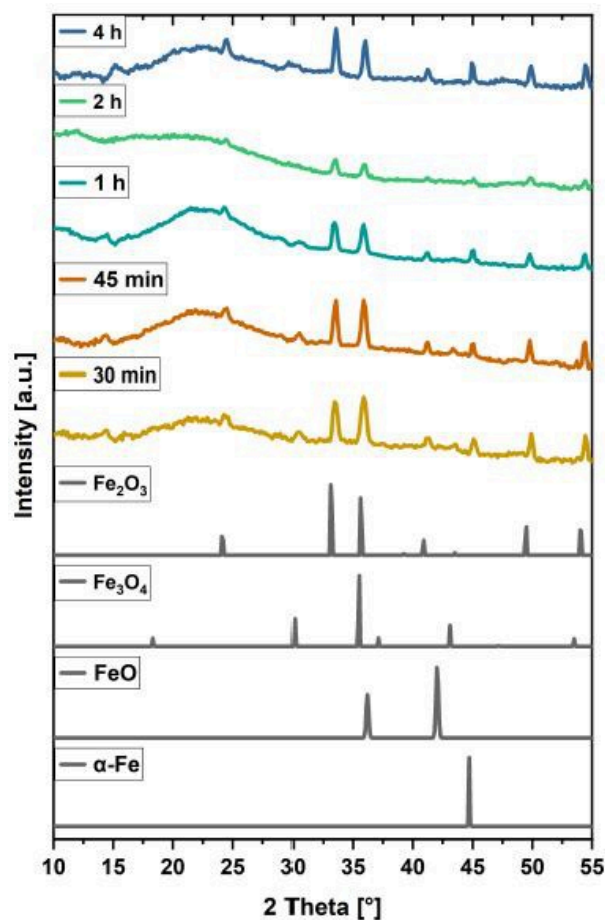


Figure 7. WAXS spectra of iron powder samples oxidized at 600°C for 30 min to 240 min and the reference spectra of α -Fe, Fe_3O_4 and α - Fe_2O_3 .

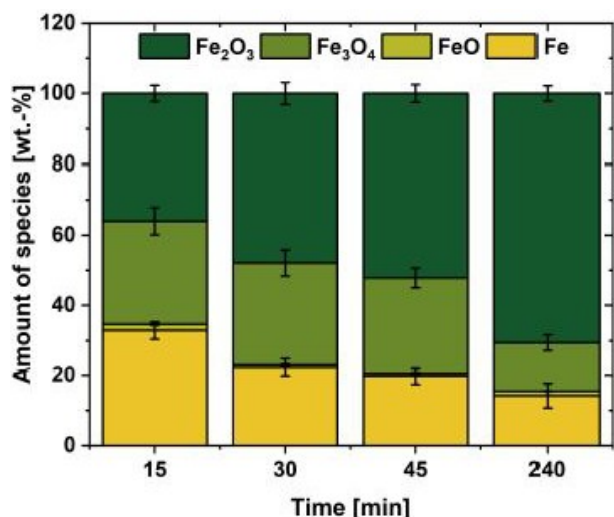


Figure 8. Phase composition of iron powder samples oxidized at 600 °C for 15 min to 240 min calculated based on Mössbauer spectroscopy.

These results reveal that the initial oxidation leads to the simultaneous formation of Fe_3O_4 and Fe_2O_3 with Fe being still present in the sample. The amount of Fe_3O_4 decreases over time before the complete consumption of iron. For temperatures above 600 °C the formation of FeO could be confirmed, but solely in small amounts. For samples obtained at higher temperatures, the oxidation was almost complete, and both Fe and FeO were fully consumed. The results obtained at 600 °C contrast with literature findings for the long-term oxidation of iron sheets, where FeO is formed as a substantial part of the oxide layer.^[29,30,37]

Similar findings for 600 °C were reported in a recent study, where FeO contributed between 2 wt.-% at 1 h and up to 8 wt.-% for 6 h oxidation time. For temperatures between 600 °C and 700 °C a higher proportion of FeO is reported.^[38] However, the layers were smaller compared to long-term oxidation of iron slabs. For the oxidation of iron slabs a ratio of 95:4:1 (FeO: Fe_3O_4 : Fe_2O_3) for layer thicknesses is reported in literature.^[29] In particle studies, a ratio of 2:2.5:3 was obtained for oxidation at 666 °C for 120 min.^[38] This distinction indicates a significant difference in the oxidation mechanism between particles and iron sheets, necessitating further investigation.

Figure 9 illustrates a schematic representation of the assumed mechanism for iron particle oxidation according to the results of the TGA, WAXS and Mössbauer analysis. The first step is the fast and initial oxidation. Here, an oxide layer formed

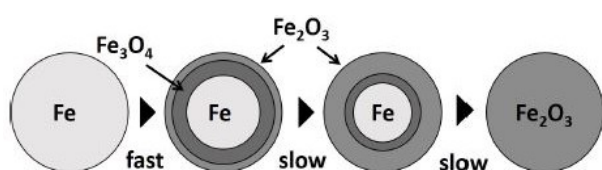


Figure 9. Schematic representation of the core-shell mechanism for the oxidation of micron-sized iron particles for temperatures below 570 °C.

consisting of Fe_2O_3 and Fe_3O_4 . The amount of oxide formed and the respective oxide layer thickness in this stage is highly dependent on the temperature as can be derived from the oxidation experiments at different temperatures and the resulting phase composition shown in Figure 4 and 5. At very high temperatures of 800 °C and 900 °C the initial oxidation can already lead to complete oxidation of the particle. For lower temperatures the next oxidation step is drastically slowed down. According to the WAXS and Mössbauer spectroscopy results of reaction intermediates, it is characterized by both the consumption of Fe_3O_4 as well as the further oxidation of the remaining iron core. The strongly decelerated reaction rate compared to the initial oxidation is due to diffusion of iron cations through the formed oxide layer being the rate-limiting step. The dominant oxidation mechanism is assumed to be the diffusion of iron cations, given their significantly smaller sizes, 0.74 Å (Fe^{2+}) and 0.64 Å (Fe^{3+}), compared to the oxygen ions (1.4 Å) within the lattice.^[39,40] Based on a numerical solution for the diffusion equation of spherical particles, a diffusion coefficient for iron of around $1 \cdot 10^{-13} \text{ m}^2 \text{ s}^{-1}$ can be estimated for oxidation at 700 °C, which agrees with results from literature.^[41]

The reaction rate of this step increases with increasing temperature as can be seen in the comparison of the oxidation at 400 °C, 500 °C, 600 °C and 700 °C (Figure 4). A possible reason is the temperature dependence of the diffusion coefficients. Another reason might be the formation of FeO at higher temperatures. A change of the reaction mechanism might lead to higher oxidation rates as the diffusion coefficient of iron cations in wüstite is higher than in magnetite.^[41]

To further verify the effect of the formed oxide shell, experiments were conducted with varying particle size. Here, the particles with an average particle diameter of 23 μm described so far and larger iron particles with average diameter of 70 μm , 119 μm and 185 μm were oxidized at 700 °C. The resulting TGA curves are shown in Figure 10.

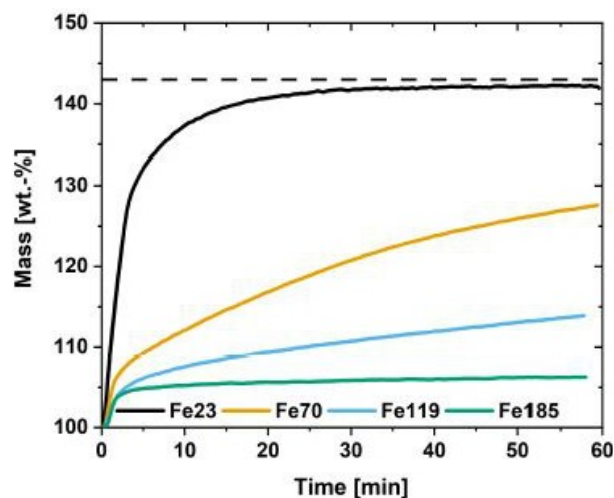


Figure 10. TGA of the isothermal oxidation of iron powder with an average particle diameter of 23 μm , 70 μm , 119 μm , 185 μm at 700 °C.

For all particle sizes the initial oxidation proceeds fast with a linear mass increase in the first minutes. Afterwards the oxidation rate is slowed down drastically. This is especially the case for the largest particles (Fe185). The initial oxidation step takes around 1.5 min and leads to approximately 4% mass increase. In the remaining oxidation process only a slight mass increase of 2% within 58.5 min is measured. The initial oxidation of sample Fe119 is comparable to sample Fe185 and leads to around 5% mass gain. However, the oxidation rate of the second stage is faster for sample Fe119. Here, the final mass increase is 14%.

For sample Fe70, both the initial oxidation and the second oxidation stage, proceed faster than for the larger particles. The initial oxidation leads to 7% mass increase which is followed by the second stage resulting in 27.5% total mass gain. This effect is more pronounced for the smallest particles Fe23. As described above, approximately 30% mass change are reached in the initial oxidation phase reacting further until nearly complete oxidation to Fe_2O_3 is reached within 60 min.

This effect can be explained by the formation of an oxide shell and the resulting change from the kinetically limited regime to the diffusion-limited regime. Here, the surface-to-volume ratio of the particles plays an important role. Assuming the formation of an oxide layer with $2.5\ \mu\text{m}$ thickness, for particles with a mean diameter of $23\ \mu\text{m}$ this corresponds to 52% of the particle being oxidized. In contrast, for a particle with a mean diameter of $185\ \mu\text{m}$, only 8% of the particle is oxidized. Thus, due to the larger surface-to-volume ratio, a larger fraction of the iron is oxidized in the initial oxidation phase, the smaller the particle diameter (Table 1).

To obtain further in-depth knowledge of the oxidation process, the morphology of the particles after oxidation was analyzed by scanning electron microscopy (SEM). The initial iron particles are depicted in Figure 17. Figure 11 illustrates iron

| | d_p [μm] | A/V [$1/\mu\text{m}$] | V_{Oxide}/V_p |
|-------|-------------------------|---------------------------|------------------------|
| Fe23 | 23.2 | 0.26 | 0.52 |
| Fe70 | 70.3 | 0.09 | 0.20 |
| Fe119 | 119.1 | 0.05 | 0.12 |
| Fe185 | 184.9 | 0.03 | 0.08 |

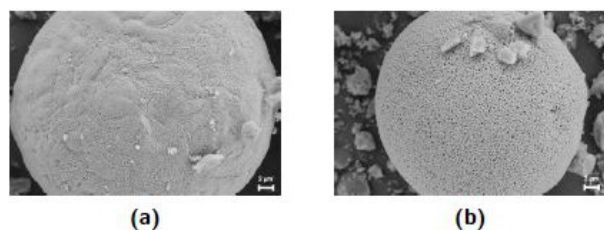


Figure 11. SEM images of iron particles with an average diameter of $23\ \mu\text{m}$ oxidized for a) 60 min at $400\ ^\circ\text{C}$ and b) 45 min at $600\ ^\circ\text{C}$. The small irregularly shaped particles are the diluent SiO_2 .

particles Fe23 oxidized for 60 min at $400\ ^\circ\text{C}$ and 45 min at $600\ ^\circ\text{C}$. It can be observed that the particles have retained their spherical shape, but the surface structure has changed. Before oxidation the iron particle surface is smooth without pores (Figure 17). The oxidation leads to the formation of a porous oxide layer. The exact structure of this porous surface depends on the temperature of isothermal oxidation as can be seen in Figure 11. The oxidation at $400\ ^\circ\text{C}$ leads to the formation of a thin oxide layer of Fe_2O_3 and Fe_3O_4 on the surface of the particle in a heterogeneous reaction. The porous structure does not cover the entire surface, as there are still areas where the surface is smooth. This indicates that iron might still be present on the surface. In comparison to this, the particle oxidized at $600\ ^\circ\text{C}$ is completely covered by an evenly porous structure.

A more detailed view on the surface of particles oxidized for one hour at different temperatures is given in Figure 12. As described above, at $400\ ^\circ\text{C}$ a fine, porous surface structure with smooth areas can be observed. The pore diameter is smaller than $0.1\ \mu\text{m}$. A completely porous surface has formed during the oxidation at $500\ ^\circ\text{C}$. The pores are slightly larger compared to the $400\ ^\circ\text{C}$ surface. Further increasing the temperature leads to a rougher, coarser surface with pores in the range of $0.5\ \mu\text{m}$ to $9.7\ \mu\text{m}$ for the samples oxidized at $600\ ^\circ\text{C}$ and $700\ ^\circ\text{C}$. Further increasing the oxidation temperature changes the particle morphology. The sample oxidized at $800\ ^\circ\text{C}$ has an irregular surface. Small areas are comparable to the samples oxidized at lower temperatures and have a porous structure. Other areas are more comparable to the sample oxidized at $900\ ^\circ\text{C}$, where a rough but non-porous, wavy surface texture can be observed.

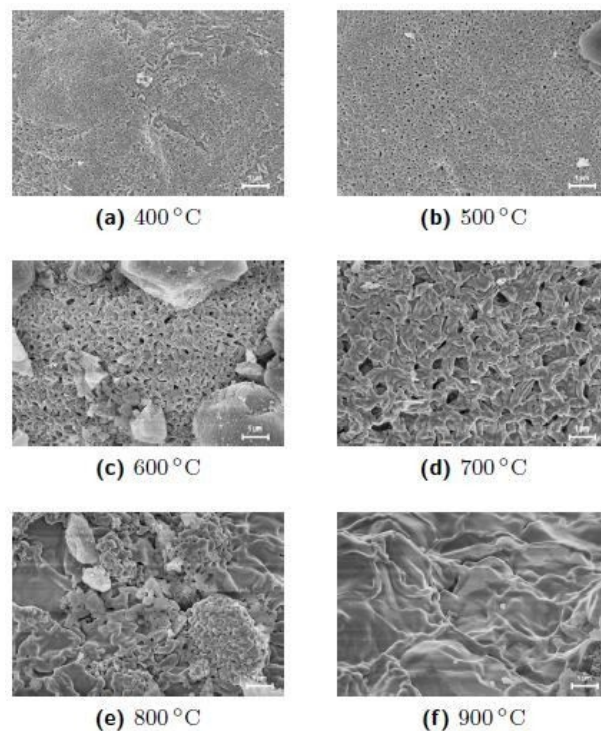


Figure 12. SEM images of the surface structure of the iron particles Fe23 oxidized for 60 min at $400\ ^\circ\text{C}$ to $900\ ^\circ\text{C}$. The brighter, irregularly shaped, small particles on the surface can be attributed to SiO_2 .

Cyclization

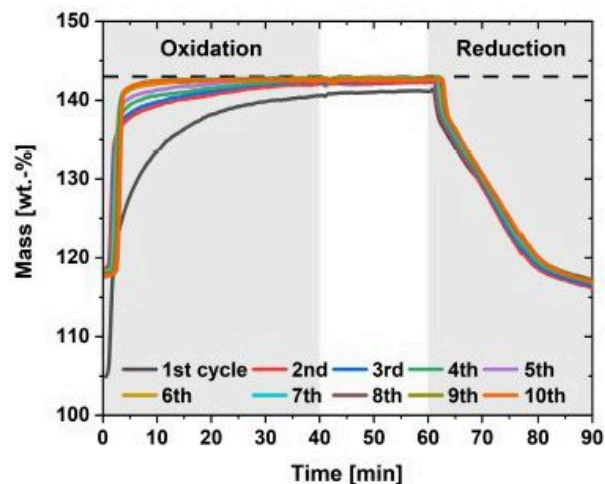
One of the most promising aspects, that promotes the utilization of iron as energy carrier, is the possibility of theoretically infinite reuse. However, as demonstrated by the earlier findings on the oxidation of iron particles, the particle morphology undergoes alterations during the oxidation process. Similarly, studies on reduction with hydrogen have indicated that the reduction process also induces changes in particle morphology.

Both oxidation and reduction are heterogeneous gas/solid reactions. It can therefore be assumed, that the particle morphology, i.e. the changing surface area or the formation of pores, has a decisive influence on the oxidation and reduction behavior of the particles. Therefore, in the following, the influence of repeated oxidation and reduction on the reaction behavior of the particles is investigated. The experiments are carried out at a temperature of 700 °C to ensure oxidation in a reasonable time frame. One cycle consists of 40 min oxidation in synthetic air, followed by 20 min purging with N₂ and 30 min reducing with 5 vol.-% to 10 vol.-% H₂ in N₂, followed by 20 min of purging with N₂.

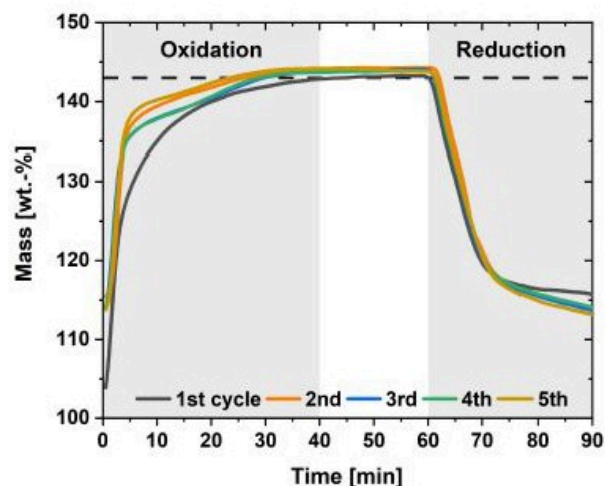
Figure 13 a) illustrates the oxidation and reduction behavior of Fe23 iron particles recycled ten times. The reduction is performed with 5 vol.-% hydrogen in N₂. The first oxidation is in line with the above shown results. The initial oxidation leads to a fast mass increase of approximately 23%. The oxidation rate is then slowed down and proceeds further until nearly complete oxidation is reached after 40 min. The oxidation behavior changes significantly with rising cycle number. However, it should be noted that the oxidation starts at a higher oxidation degree from the second cycle on. It can be observed that the oxidation rate increases from the first to the sixth cycle.

With rising cycle number the amount of sample oxidized in the initial oxidation phase increases. From the sixth cycle on, oxidation is completed in the initial phase within a few minutes. In contrast to that, the reduction proceeds in the same course for each cycle. The reduction can be divided into three stages. The first stage takes approximately one minute and is characterized by a fast reduction resulting in around 4% mass decrease. In the second reduction stage, the reduction rate is slower, in approximately 20 min around 19% of the mass is lost. The third stage is characterized by a strongly decelerated reduction rate. Here, a reduction time of 10 min does solely lead to a further mass decrease of 2%. Thus, with a reduction time of 30 min an overall mass decrease of 25% can be reached.

To further analyze the reduction behavior of oxidized iron particles, additional cycling experiments were performed with 10 vol.-% hydrogen in N₂. The resulting TGA curves are depicted in Figure 13 b). Since the focus of these experiment is on the reduction, which hardly differs between different cycles, only five cycles were performed. Reducing with 10 vol.-% hydrogen changes the reduction from a three stage process to a two stage process. The first stage is again characterized by a very fast reaction rate, which is, in comparison to the reduction with 5 vol.-%, not slowed down after one minute. It takes around



(a)



(b)

Figure 13. Cyclization of powder sample Fe23 at 700 °C. The oxidation is conducted in synthetic air and the reduction with a) 5 vol.-% H₂ in N₂ and b) 10 vol.-% H₂. Between each oxidation and reduction step the reactor is purged with N₂ for 20 min.

10 min and leads to a mass decrease of 26%. The subsequent course of the reaction is controlled by a strongly decelerated reduction rate. 4% mass decrease are reached in the remaining 20 min reduction time. With 10 vol.-% H₂, a slightly higher reduction degree can be achieved in comparison to 5 vol.-% H₂. The reduction of the oxides with 10 vol.-% H₂ has a negligible influence on the course of the oxidation. The slight deviation between the maximum achieved mass increase and the theoretical maximum value of 143% can be ascribed to experimental measurement errors. The oxidation rate of the initial oxidation is comparable for all cycles. However, from the third cycle onwards, a minimal change in the course of the oxidation can be observed. The final mass gain of the initial oxidation is slightly lower for the sample reduced with 10 vol.-%

% H₂. In the fifth cycle, the initial oxidation leads to almost complete oxidation (142%) for the 5 vol.-% H₂ sample while the 10 vol.-% H₂ sample reaches around 137%. The oxidation rate is then decreased, but complete oxidation is also achieved after 30 min, as with cyclization with 5 vol.-% H₂.

In addition to the effect of the hydrogen content, the effect of the particle size was investigated. Cyclization experiments with up to five cycles and the same experimental conditions as for powder sample Fe23 were performed for iron particles with an average diameter of 70 μm (Fe70). The results are shown in Figure 14. The increased particle size leads to strongly decelerated reaction rates. In the first cycle a final mass gain of 27% is reached.

The effect on the subsequent reduction is even more pronounced. Here, a mass decrease of solely 5% due to reduction can be observed. Thus, the next oxidation starts at 122%. The oxidation rate increases with increasing cycle number, consistent with observations in cyclization experiments with smaller particles. In the fifth cycle a final mass gain of around 41% is reached. The reduction can be divided into three stages, a fast initial reduction, a slightly decreased reduction leading to the highest reduction progress and a third, strongly decelerated step, where the degree of reduction hardly changes. The initial reduction stage is comparable for all five cycles, whereas the length of the second reduction stage increases with rising cycle number. Nevertheless, the final mass change reached by reduction is the same for all cycles from the second cycle on. It is 124% with respect to the initial iron mass. Similar observations for the reduction of combusted iron particles were made by Hessels et al.^[42] They found that the course of the reduction changes for reduction temperatures higher than 600 °C compared to lower temperatures. At low temperatures they found a slow, but progressing reduction while for $T > 600$ °C the reduction is characterized by a sharply decreased reaction rate comparable to the findings in this work. They suggested that the reduction is slowed down due to the formation of FeO and a change of the reaction mechanism from

boundary controlled to limitation by nucleation and growth. To verify this hypothesis for the cyclization case, Mössbauer spectroscopy was performed for both samples Fe70 and Fe23 obtained after five cycles. The resulting phase composition is shown in Figure 15. This analysis demonstrates the formation of FeO in both cases. Both samples consists of a mixture of Fe, Fe₃O₄ and FeO. The reduction extent of sample Fe23 is higher due to the smaller particle size. It consists of 50% iron, 33% Fe₃O₄ and around 17% FeO. The amount of iron in the Fe70 sample is with 33% lower while the amount of oxide with 47% Fe₃O₄ and 21% FeO is higher. The phase composition suggests that the reduction of iron oxide particles is a multi step mechanism with the simultaneous formation of the various iron oxides and iron. Here, a core-shell mechanism might also be suitable. The initial reduction might lead to the formation of a dense iron layer, leading to a decreased reduction rate due to diffusion limitations. With proceeding reduction the thickness of the iron layer grows, further delaying the reduction. However, a more detailed analysis of the reduction process of oxidized iron particles would be necessary to completely understand the process, e.g. analysis of reaction intermediates or in-situ studies. This was not part of this work but will be addressed in future.

As described above, the course of oxidation for all the cyclization experiments depicted here changes with increasing number of cycles. Since the degree of reduction achieved by the reduction does not change from cycle to cycle and thus the starting point of the subsequent oxidation is nearly the same from the second cycle on, it is assumed that the change of the oxidation behavior is not caused by a variation of the phase composition. It is postulated that a change of the surface morphology might influence the oxidation behavior. To analyze the change of the particle morphology SEM images were recorded of a sample after one and ten cycles (Figure 16). It can be observed that the particle becomes porous due to reduction. The surface structure of the reduced particles differs significantly from the surface structure of the oxidized particles

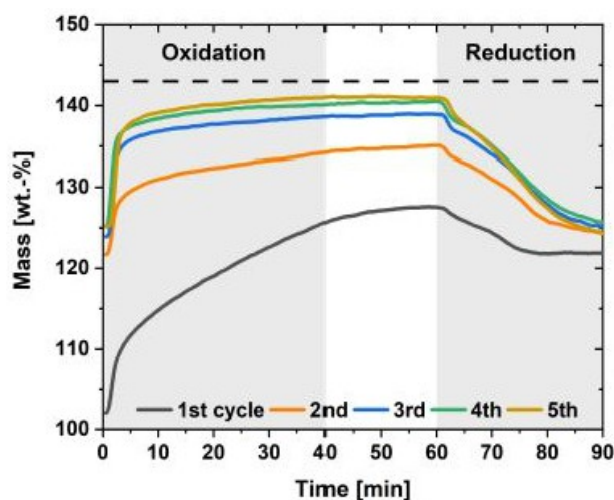


Figure 14. Cyclization of powder sample Fe70 at 700 °C. The oxidation is conducted in synthetic air and the reduction with 5 vol.-% H₂ in N₂.

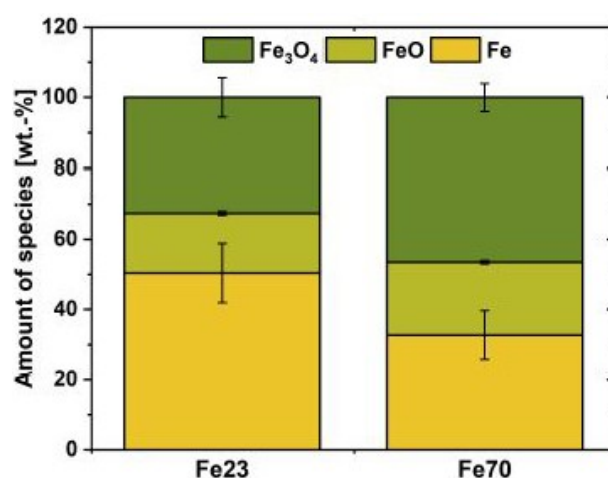


Figure 15. Phase composition of sample Fe23 and Fe70 obtained after five oxidation and reduction cycles calculated based on Mössbauer spectroscopy.

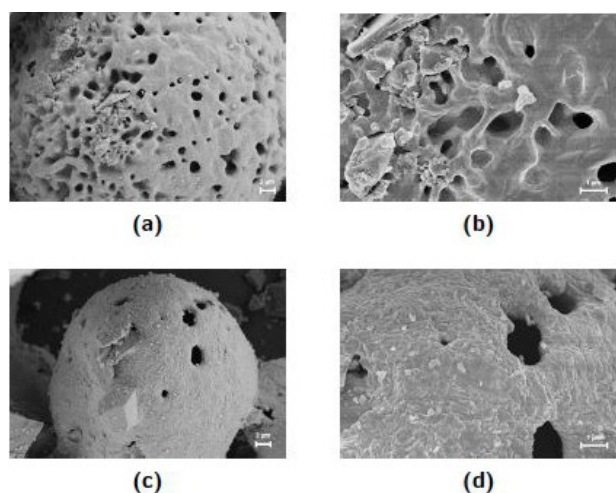


Figure 16. SEM images of the iron particles Fe23 after one (a, b) and after ten cycles (c, d). The brighter, irregularly shaped, small particles on the surface can be attributed to SiO_2 .

(Figure 12d)). After one oxidation and reduction cycle there exists a large number of pores with a diameter smaller than $1\ \mu\text{m}$. Both more superficial pores and deeper pores can be distinguished. Figure 16c) and d) shows SEM images of an iron particle cycled ten times. Here, less, but slightly larger pores are visible. However, these pores seem to reach deep inside the particle. Due to the increased porosity, a larger surface area is available for the heterogeneous reaction, therefore the reaction rate increases with the number of cycles. This effect is less pronounced for the reduction due to the higher diffusivity of hydrogen. Sepman et al.^[43] investigated repeated combustion at high temperatures followed by reduction with hydrogen. This investigation also revealed alterations in morphology and an increase of the specific surface area due to cyclization. However, the high-temperature combustion resulted in melting and partial vaporization of iron, reducing the porosity created during reduction. Consequently, the impact of morphological changes was less significant compared to the milder conditions examined in this study.

Conclusions

The oxidation behavior of iron particles was investigated based on thermogravimetric analysis for a wide range of experimental conditions, i.e. variation of heating rates, isothermal temperature and use of different particle size distributions. The oxidation rate is strongly dependent on the particle size and the oxidation temperature. The obtained results indicate, that the oxidation process is a core-shell mechanism which can be divided into two stages. The fast initial oxidation leads to the formation of an iron oxide shell. The subsequent step is then characterized by the outwards diffusion of iron cations being the rate limiting-step and leading to a strong decrease of the oxidation rate. To accelerate the rate-determining step, small particles ($d_p < 30\ \mu\text{m}$) and high temperatures ($T \geq 700\ ^\circ\text{C}$) are

preferable. In addition to the oxidation, the influence of cyclization on the reaction behavior of iron particles was investigated. The results indicate that cyclization of iron particles is feasible and enhances reactivity. In the cycling experiments with up to ten cycles, both the oxidation and reduction rates increase with increasing cycle number with a more significant effect on the oxidation rate. Based on SEM analysis, it could be shown that this effect is likely due to an increased porosity of the particles. However, no complete reduction could be reached with the investigated experimental parameters, which might be due to the formation of FeO. Thus, future work is required focusing on the reduction of oxidized iron particles for a detailed understanding of the reduction process and the influence of FeO, e.g. by analysis of reaction intermediates and in-situ experiments.

Experimental

Fresh Iron Powder

Different iron powder batches with various average particle diameters were used (*Eckart TLS* and *Pometon*). The average particle diameters of the analyzed powders are $23\ \mu\text{m}$, $70\ \mu\text{m}$, $119\ \mu\text{m}$ and $185\ \mu\text{m}$. Details on the particle size distribution can be found in the supplementary material (Figure S1). The properties of the iron powders are summarized in Table 2. Scanning electron microscopy images are shown in Figure 17. The powder samples Fe23, Fe70 and Fe119 consist of spherical particles with a smooth surface (Figure 17a–f)). In comparison, the particles of sample Fe185 are irregularly shaped with deep indentations.

Thermogravimetric Analysis

The oxidation of iron powder was studied in a series of thermogravimetric experiments with a Netzsch STA409. The non-isothermal experiments were performed at three different heating rates ($2\ \text{Kmin}^{-1}$, $5\ \text{Kmin}^{-1}$, $10\ \text{Kmin}^{-1}$) for temperatures up to $1200\ ^\circ\text{C}$ with synthetic air. The volume flux was set to $100\ \text{mLmin}^{-1}$.

For the isothermal experiments, the sample was heated in nitrogen atmosphere ($200\ \text{mLmin}^{-1}$) up to the target temperature. Once the temperature was reached, the gas supply was automatically switched from nitrogen to synthetic air ($100\ \text{mLmin}^{-1}$). In addition to the oxidation experiments, cyclization with up to ten cycles of oxidation followed by reduction was investigated at $700\ ^\circ\text{C}$. For this purpose, the powder sample was heated in nitrogen atmosphere. After reaching the desired temperature the sample was oxidized for 40 min with a flow rate of $100\ \text{mLmin}^{-1}$ of synthetic air and reduced for 30 min with 5 vol.-% or 10 vol.-% H_2 in N_2 with a flow rate of $100\ \text{mLmin}^{-1}$. Each oxidation and reduction was followed by 20 min purging with $200\ \text{mLmin}^{-1}$ of N_2 .

Table 2. Properties of the analyzed iron powders.

| | average particle diameter [μm] | particle size distribution [μm] | manufacturer |
|-------|---|--|--------------|
| Fe23 | 23.2 | < 32 | Eckart TLS |
| Fe70 | 70.3 | 45 to 100 | Eckart TLS |
| Fe119 | 119.1 | 100 to 150 | Eckart TLS |
| Fe185 | 184.9 | 60 to 425 | Pometon |

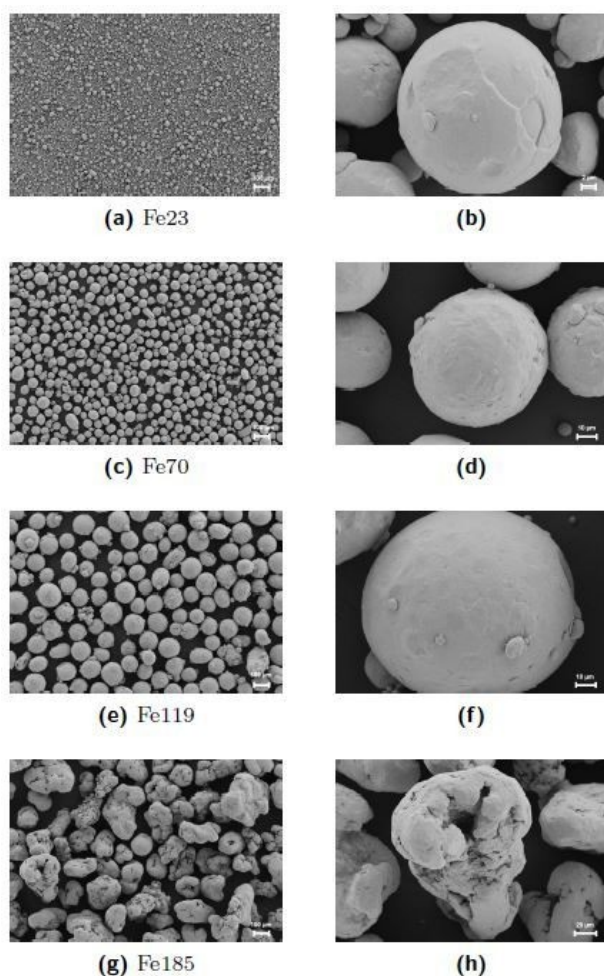


Figure 17. SEM images of the iron particles used in this study.

First thermogravimetric experiments of the oxidation of Fe₂₃ with a heating rate of 10 K/min revealed incomplete oxidation to Fe₂O₃, although reaching temperatures of up to 1200 °C (Figure 18). A strong decrease of the reaction rate for temperatures above 700 °C can be observed. Analysis of the powder after oxidation showed strong agglomeration and sintering of the individual particles. This leads to a decelerated reaction rate due to diffusion limitations.^[38] To eliminate the influence of sintering on the reaction process, the iron powder was diluted with ball-milled SiO₂ (Merck). Dilution with SiO₂ can successfully prevent sintering at higher temperatures as depicted in Figure 18. The use of SiO₂ as diluent has limited practical relevance. Its primary function is to enhance the understanding of the processes involved by mitigating the effects of sintering. For each experiment 25 ± 3 mg iron powder was used. For iron diluted with SiO₂ in a mass ratio of 1:2, a final mass increase of 38% can be observed. This corresponds to the mass increase for complete conversion of iron to Fe₃O₄. However, the oxidized sample were still agglomerated. This observation suggests that sintering was limited, but that better separation of the particles is needed. For iron with a dilution in a mass ratio of 1:4, a mass increase of 41% was observed at 1000 °C, which is 2% below the theoretical maximum mass increase of 43% for complete oxidation to Fe₂O₃. However, analysis of the oxidized sample by WAXS confirmed complete oxidation to Fe₂O₃. The deviations of up to 2% from the theoretically achievable mass change can be attributed to measurement errors due to the buoyancy effect, although a

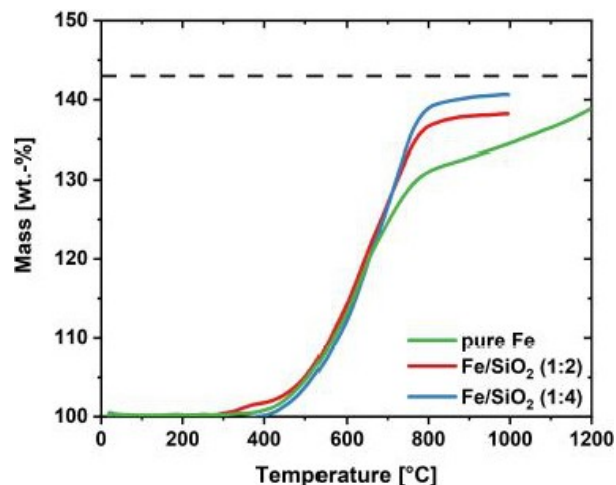


Figure 18. Oxidation of pure iron with a heating rate of 10 K min⁻¹ in comparison to diluted powder samples with an iron to SiO₂ mass ratio of 1:2 and 1:4. The dashed line marks the theoretical mass gain reached by complete oxidation to Fe₂O₃.

correction measurement was performed for each experiment. Thus, all further experiments are performed with a Fe to SiO₂ mass ratio of 1:4. An exception are the measurements for which the samples were analyzed by WAXS. Here, amorphous SiO₂ (Sigma-Aldrich, -325 mesh) was used to avoid additional sharp peaks in the diffractogram due to crystalline SiO₂. Since amorphous SiO₂ has a lower density than crystalline SiO₂, these experiments were performed with a mass ratio of 1:3. The SiO₂ used, crystalline or amorphous, has no influence on the course of the reaction (ESI, Figure S2). In addition, an influence of the crucible type on the reaction behavior, flat or cylindrical, could be excluded (ESI, Figure S2). It is assumed that the crucible material has no influence on the reaction.

Wide-Angle X-ray Scattering (WAXS)

When radiation impinges upon a crystal, reflection can occur at the lattice planes of the crystal lattice. According to Bragg's law, this results in angle-dependent interference when the path difference is a multiple of the radiation's wavelength. These angle-dependent interference peaks, called Bragg peaks, are specific to the crystal and can be evaluated for quantitative and qualitative analysis. The scattering experiments were conducted using a Xeuss 2.0 Q-Xoom (Xenocs SA, Grenoble, France). The X-ray radiation is produced by an X-ray source (GeniX 3D Cu ULD) which emits Cu-K_α radiation that passes a collimation assembly. The collimated beam with a wavelength of 1.5406 Å is directed through the sample positioned within a vacuum chamber to minimize background radiation. Consequently, the scattered radiation of each sample is measured using a Pilatus3 R 300k detector (Dectris Ltd., Baden-Dättwil, Switzerland) with an exposure time of 30 min. All powder samples were deposited on an adhesive polyimide film, positioned at a distance of 80 mm from the detector. As a result of the conducted experiments the scattered intensity *I* is plotted as a function of the scattering angle 2θ.

Mössbauer Spectroscopy

⁵⁷Fe Mössbauer spectroscopy was performed in transmission geometry at room temperature with a setup from Halder instruments, equipped with a proportional counter and a CMCA-500

Table 3. Lamb-Mössbauer f-factors.^[38]

| Species | f_i |
|--------------------------------|-------|
| Fe ₂ O ₃ | 0.84 |
| Fe ₃ O ₄ | 0.93 |
| FeO | 0.8 |
| Fe | 0.8 |

(combined multi-channel analyzer, Wissel). The ⁵⁷Co/Rh source was moved in a triangular waveform and had an initial activity of 100 mCi. The source was continuously kept at room temperature. A standard 25 μm α-iron foil was used for calibration. Sample loadings were in line with the ideal loading approximations by Long et al.^[44,45] Data treatment was performed with the MossA software package.^[46] The extraction of the phase compositions from the Mössbauer spectral areas is based on Equation 1 with the help of the Lamb-Mössbauer factors (LMF, f_i) given in Table 3.^[38] In the context of the thin absorber approximation, the spectral area A_i of a component i is proportional to its area density of the ⁵⁷Fe-atoms and its LMF f_i . Weighting A_i with f_i , the molar Mass M_i , the stoichiometric factor for iron atoms ν_i in the component and putting it in relation with the contributions of all components j in the sample enables its weight-based quantification (Equation 1).^[47] The unit of $m_{i,\%}$ is wt.-%.

$$m_{i,\%} = \frac{\frac{A_i}{f_i \nu_i} \cdot M_i}{\sum_j \left(\frac{A_j}{f_j \nu_j} \cdot M_j \right)} \cdot 100 \quad (1)$$

The respective Mössbauer fits can be found in the supplementary material (Figure S5, S6, S7). The fit parameter are reported in Tab. S4 and S5.

Acknowledgements

This work was performed within the cluster project Clean Circles. Financial support by the Strategy Fund of the KIT Presidium is gratefully acknowledged. J.S. and U.I.K. acknowledge financial support by the Hessian Ministry of higher Education, Research, Science and the Arts. We thank Lara Kuhnert (EST, Technical University Darmstadt) for performing the particle size distribution analysis. Open Access funding enabled and organized by Projekt DEAL.

Conflict of Interests

The authors declare no conflict of interest.

Data Availability Statement

The data that support the findings of this study are available from the corresponding author upon reasonable request.

Keywords: Metal fuels · Iron · Energy storage · Oxidation · Cyclization · Particle Morphology

- [1] K. Mazloomi, C. Gomes, *Renew. Sustain. Energy Rev.* **2012**, *16*, 3024.
- [2] J. Andersson, S. Grönkvist, *Int. J. Hydrogen Energy* **2019**, *44*, 11901.
- [3] Q. Lai, M. Paskevicius, D. A. Sheppard, C. E. Buckley, A. W. Thornton, M. R. Hill, Q. Gu, J. Mao, Z. Huang, H. K. Liu, Z. Guo, A. Banerjee, S. Chakraborty, R. Ahuja, K.-F. Aguey-Zinsou, *ChemSusChem* **2015**, *8*, 2789.
- [4] N. Armaroli, V. Balzani, *ChemSusChem* **2011**, *4*, 21.
- [5] J. M. Bergthorson, *Prog. Energy Combust. Sci.* **2018**, *68*, 169.
- [6] H. Wiinikka, T. Vikström, J. Wennebro, P. Toth, A. Sepman, *Energy Fuels* **2018**, *32*, 9982.
- [7] S. H. Fischer, M. C. Grubelich, *Technical Report* **1998**.
- [8] K. T. Møller, T. R. Jensen, E. Akiba, H.-W. Li, *Prog. Nat. Sci.-Mater.* **2017**, *27*, 34.
- [9] Y. Li, H. Chen, X. Zhang, C. Tan, Y. Ding, *Appl. Therm. Eng.* **2010**, *30*, 1985.
- [10] C. Zamfirescu, I. Dincer, *J. Power Sources* **2008**, *185*, 459.
- [11] J. M. Bergthorson, S. Goroshin, M. J. Soo, P. Julien, J. Palecka, D. L. Frost, D. J. Jarvis, *Appl. Energy* **2015**, *160*, 368.
- [12] J. Janicka, P. Debiagi, A. Scholtissek, A. Dreizler, B. Epple, R. Pawellek, A. Maltsev, C. Hasse, *Appl. Energy* **2023**, *339*, 120950.
- [13] C. Hessels, A. Smeets, G. Finotello, N. G. Deen, Y. Tang, *Particuology* **2023**, *83*, 8.
- [14] Q. Fradet, M. L. Ali, U. Riedel, *Steel Res. Int.* **2022**, *93*.
- [15] S. D. Angeli, S. Gossler, S. Lichtenberg, G. Kass, A. K. Agrawal, M. Valerius, K. P. Kinzel, O. Deutschmann, *Angew. Chem. Int. Ed.* **2021**, *60*, 11852.
- [16] P. Blanck, G. Kass, K. P. Kinzel, O. Deutschmann, *Energy Adv.* **2024**, *3*, 123–130.
- [17] P. Debiagi, R. C. Rocha, A. Scholtissek, J. Janicka, C. Hasse, *Renewable Sustainable Energy Rev.* **2022**, *165*, 112579.
- [18] C. Kuhn, A. Düll, P. Rohlf, S. Tischer, M. Börnhorst, O. Deutschmann, *Appl. Energy Combust. Sci.* **2022**, *12*, 100096.
- [19] J. Neumann, R. C. Da Rocha, P. Debiagi, A. Scholtissek, F. Dammel, P. Stephan, C. Hasse, *Appl. Energy Combust. Sci.* **2023**, *14*, 100128.
- [20] L. Dirven, N. G. Deen, M. Golombok, *Sustain. Energy Technol. Assess.* **2018**, *30*, 52.
- [21] M. E. Diego, J. C. Abanades, *Chem. Eng. J.* **2022**, *428*, 132083.
- [22] L. F. Calvo, G. Grasa, M. Alonso, M. E. Diego, *Fuel Process. Technol.* **2023**, *245*, 107755.
- [23] M. Wokon, A. Kohzer, M. Linder, *Sol. Energy* **2017**, *153*, 200.
- [24] Q. Lei, Q. Si, J. Zhang, Y. Jiang, L. Hu, L. Qiao, X. Zu, G. Xiao, J. Yang, S. Li, *Appl. Energy* **2022**, *305*, 117958.
- [25] S. Buchheiser, M. P. Deutschmann, F. Rhein, A. Allmang, M. Fedoryk, B. Stelzner, S. Harth, D. Trimis, H. Nirschl, *Materials* **2023**, *16*.
- [26] L. Choisez, N. E. van Rooij, C. J. Hessels, A. K. Da Silva, I. R. S. Filho, Y. Ma, P. de Goey, H. Springer, D. Raabe, *Acta Mater.* **2022**, *239*, 118261.
- [27] M. Baigmohammadi, W. Prasadha, N. C. Stevens, Y. L. Shoshyn, T. Spee, P. de Goey, *Appl. Energy Combust. Sci.* **2023**, *13*, 100116.
- [28] X. Mi, A. Fujinawa, J. M. Bergthorson, *Combust. Flame* **2022**, *240*, 112011.
- [29] R. Chen, W. Yeun, *Oxid. Met.* **2003**, *59*, 433.
- [30] B. Pujilaksono, T. Jonsson, M. Halvarsson, J.-E. Svensson, L.-G. Johansson, *Corros. Sci.* **2010**, *52*, 1560.
- [31] J. Païdassi, *Acta Metall.* **1958**, *6*, 219.
- [32] E. N. Lysenko, E. V. Nikolaev, V. A. Vlasov, S. P. Zhuravkov, *Iop. Conf. Ser. Mater. Sci. Eng.* **2016**, *110*, 012093.
- [33] A. V. Korshunov, *Russ. J. Phys. Chem. B* **2012**, *6*, 368.
- [34] E. N. Lysenko, A. P. Surzhikov, S. P. Zhuravkov, V. A. Vlasov, A. V. Pustovalov, N. A. Yavorovsky, *J. Therm. Anal. Calorim.* **2014**, *115*, 1447.
- [35] C. M. Zhang, J. Jin, D. D. He, H. Zhang, J. Jiang, X. Y. Gao, W. J. Gao, *Adv. Mater. Res.* **2012**, *535–537*, 459.
- [36] N. Bertrand, C. Desgranges, D. Poquillon, M. C. Lafont, D. Monceau, *Oxid. Met.* **2010**, *73*, 139.
- [37] L. Yuan, R. Cai, J. I. Jang, W. Zhu, C. Wang, Y. Wang, G. Zhou, *Nanoscale* **2013**, *5*, 7581.
- [38] J. Spielmann, D. Braig, A. Streck, T. Gustmann, C. Kuhn, F. Rainauer, A. Kurnosov, O. Leubner, V. Potapkin, C. Hasse, O. Deutschmann, B. J. Etzold, A. Scholtissek, U. I. Kramm, *Phys. Chem. Chem. Phys.* **2024**, *26*, 13049–13060.
- [39] Z. Ma, K. Wu, H. Wang, L. Zhu, Z. Li, Y. Luo, Y. Lu, *Fuel* **2023**, *331*, 125699.
- [40] F. Li, Z. Sun, S. Luo, L.-S. Fan, *Energy Environ. Sci.* **2011**, *4*, 876.
- [41] L. Himmel, R. F. Mehl, C. E. Birchenall, *JOM* **1953**, *5*, 827.

- [42] C. Hessels, T. Homan, N. G. Deen, Y. Tang, *Powder Technol.* **2022**, *407*, 117540.
- [43] A. Sepman, J. S. Malhotra, J. Wennebro, H. Wiinikka, *Combust. Flame* **2024**, *259*, 113137.
- [44] G. J. Long, T. E. Cranshaw, G. Longworth, *Mössbauer Eff. Ref. Data J.* **1983**, *6*, 42.
- [45] F. Grandjean, G. J. Long, *Chem. Mater.* **2021**, *33*, 3878.
- [46] C. Prescher, C. McCammon, L. Dubrovinsky, *J. Appl. Crystallogr.* **2012**, *45*, 329.
- [47] W. Meisel, G. Kreysa, *Z. Anorg. Allg. Chem.* **1973**, *395*, 31.

Manuscript received: February 19, 2024
Revised manuscript received: April 23, 2024
Accepted manuscript online: May 3, 2024
Version of record online: June 10, 2024
